Eur. Phys. J. Plus (2026) 141:508
https://doi.org/10.1140/epjp/s13360-026-07677-7

THE EUROPEAN
PHYSICAL JOURNAL PLUS

Regular Article

Microwave-tunable vacuum-induced photonic spin hall effect in a Δ-system

Muqaddar Abbas[1,a], **Hamid R. Hamedi**[2,b]

[1] Department of Foundation Teaching and Research, Shenyang Urban Construction University, Shenyang 110167, China
[2] Institute of Theoretical Physics and Astronomy, Vilnius University, Sauletekio 3, Vilnius 10257, Lithuania

Received: 2 December 2025 / Accepted: 9 April 2026

Abstract We investigate the photonic Spin Hall Effect (PSHE) in an optical cavity containing a Δ-type three-level atomic ensemble, where transparency is generated intrinsically by the quantized cavity vacuum field through vacuum-induced transparency (VIT). Building on this mechanism, we introduce and analyze a vacuum-induced PSHE, in which the transverse spin-dependent shift of the reflected probe beam arises solely from vacuum–atom coupling, thereby strengthening the underlying spin–orbit interaction. We further demonstrate that applying a weak microwave field to the lower atomic transition enables active, high-precision tuning of the vacuum-induced PSHE magnitude. The displacement is also shown to depend sensitively on the intracavity photon number, providing an additional degree of quantum control over spin-resolved beam dynamics. Finally, we extend our study to include Doppler broadening, revealing how thermal motion modifies the susceptibility and alters the characteristic spin-dependent shifts. The combined results uncover key aspects of vacuum-mediated light–matter interactions in Δ-systems and establish a versatile framework for manipulating the PSHE in cavity-based quantum electrodynamics platforms.

1 Introduction

Quantum coherence plays a fundamental role in tailoring the optical response of atomic systems, particularly in phenomena like electromagnetically induced transparency (EIT) [1, 2]. In a prototypical Λ-type three-level atom, EIT emerges when a weak probe field interacts with one optical transition, while a strong classical control field couples a second transition, leading to quantum interference that suppresses absorption. More recently, this interference-based transparency has been explored in regimes where the control field is quantized, especially within high-finesse optical cavities [2]. In such configurations, even a few photons or in the extreme case, a vacuum field can induce transparency, known as vacuum-induced transparency (VIT) [3, 4], enabled by strong coupling between atoms and cavity modes.

Quantum coherence effects arising from the interaction between atomic systems and the vacuum fluctuations of the electromagnetic field have garnered significant attention, both theoretically and experimentally. These vacuum-mediated interactions lead to a variety of distinctly quantum phenomena, including vacuum Rabi splitting [4–8], vacuum-induced transparency [3, 9], and vacuum-induced coherence [10]. Moreover, the influence of vacuum fluctuations has been observed in processes such as the alteration of four-wave mixing [11], the development of vacuum-based quantum memories [12, 13], and well-known quantum electrodynamic effects like the Lamb shift [14] and spontaneous emission [15].

In the framework of EIT, cavity-assisted configurations have been shown to be highly sensitive to the quantum nature of the intracavity field [16]. Notably, even in the absence of real photons in the control mode, i.e., when the cavity field remains in the vacuum state, transparent behavior can still be observed in a strongly coupled atom-cavity system comprising three-level atoms [3, 4]. This highlights the essential role of vacuum-induced coherence in controlling light propagation in quantum optical systems.

A significant step toward deepening our understanding of spin-dependent light–matter interactions has been the discovery and study of the photonic spin Hall effect (PSHE), now recognized as a central phenomenon in contemporary spin photonics. The PSHE is characterized by a polarization-dependent transverse shift of an optical beam, in which left- as well as right-circularly polarized components undergo transverse displacements of equal magnitude but opposite direction when interacting with structured or inhomogeneous media. This phenomenon arises from the intrinsic spin–orbit coupling (SOC) of light and constitutes the optical analog of the electronic spin Hall effect extensively studied in condensed-matter systems [17, 18]. Unlike its electronic counterpart, where spin-polarized charge carriers are deflected under an external electric field, the PSHE replaces electrons with circularly polarized photons, and the role of the electric potential gradient is assumed by spatial variations in refractive index or interface

---

[a] e-mail: muqaddarabbas@outlook.com

[b] e-mail: hamid.hamedi@tfai.vu.lt (corresponding author)

geometry [19, 20]. Originally predicted by Onoda et al. in 2004 [17], the effect was subsequently formalized by Bliokh and Bliokh [18], who emphasized the significance of both geometric and dynamical phases in governing spin-dependent optical shifts.

The PSHE emerges fundamentally from the intrinsic spin–orbit interaction of light, wherein the spin angular momentum (SAM) of photons couples with their spatial degrees of freedom. This interplay is underpinned by the conservation of total angular momentum in electromagnetic systems [21, 22]. As a result, circularly polarized photons, representing opposite spin states, undergo lateral displacements in opposite directions when interacting with refractive index gradients or structured interfaces [23].

These spin-dependent deflections are not merely a consequence of material boundaries, but are strongly modulated by the angular momentum content and the acquisition of geometric phases during light propagation [24]. Two distinct types of geometric phase play crucial roles in this context. The first contribution is the spin-redirection phase, also known as the Rytov–Vlasimirskii–Berry phase, which emerges from the continuous variation in the propagation direction of light. The second contribution is the Pancharatnam–Berry phase, arising from the evolution of the polarization state and induced through polarization transformations [24, 25].

The PSHE has become a fundamental tool for investigating spin-dependent light–matter interactions, with various atomic configurations offering significant insights into its underlying mechanisms [26–31]. On the other hand, recently, several vacuum-induced optical phenomena, including vacuum-induced gratings and vacuum-induced Goos–Hänchen shifts have been explored within the framework of VIT [32, 33]. Despite these advances, the PSHE has not yet been studied in the context of VIT. In this work, we fill this gap by demonstrating a microwave tunable vacuum-induced PSHE in a Δ-type atomic system, thereby extending the scope of previous investigations.

In this work, we advance the exploration of vacuum-mediated light–matter interactions by proposing and analyzing a microwave tunable vacuum-induced PSHE in a Δ-type atomic system embedded inside an optical cavity. In contrast to conventional schemes that rely on classical control beams [26–31], the transverse spin-dependent displacement of the reflected probe field in our configuration originates from the intrinsic coupling between the atoms and the quantized vacuum mode. This mechanism naturally enhances spin–orbit interaction and allows the PSHE to emerge without any externally applied optical control. We also show that the addition of a weak microwave field acting on the lower atomic transition provides a powerful means of tuning in both the strength and sign of the vacuum-induced PSHE, while the intracavity photon number offers a complementary route for regulating spin-dependent beam shifts at the quantum level. Furthermore, by incorporating Doppler broadening into our model, we assess how thermal motion modifies the cavity susceptibility and influences the resulting spin-dependent deflection, thereby bridging the gap between idealized cold-atom predictions and experimentally relevant room-temperature conditions. Altogether, our study establishes a versatile framework for engineering and controlling PSHE through vacuum-induced coherence, microwave driving, and thermal atom dynamics, opening new opportunities for quantum photonic devices and cavity-QED–based information processing.

Unlike recent studies of microwave-controlled PSHE in classically driven Λ-type media [34], the present work considers a cavity-assisted Δ-type system in which the relevant transparency mechanism is vacuum-induced transparency generated by the quantized cavity mode. As a result, the PSHE studied here is fundamentally vacuum-mediated and can arise even in the absence of an externally applied classical optical control field. In addition, the present framework enables us to examine the roles of intracavity photon number and Doppler broadening, which provide further quantum and thermal control of the spin-dependent transverse shift.

2 System description

We consider a three-level atomic configuration realized with rubidium-87 (^{87}Rb) atoms placed inside an optical cavity. The atomic ensemble is simultaneously driven by three fields: a single-mode cavity field, a weak probe beam, and an externally applied microwave field, as illustrated in Fig. 1(a). Specifically, the cavity mode couples the states $|c\rangle$ and $|b\rangle$, the probe field excites the transition between $|c\rangle$ and $|a\rangle$, while the microwave field links the states $|a\rangle$ and $|b\rangle$. The chosen energy levels correspond to $|a\rangle = |5S_{1/2}, F = 1\rangle$, $|b\rangle = |5S_{1/2}, F = 2\rangle$, and $|c\rangle = |5P_{3/2}, F = 2\rangle$.

The evolution of the system is governed by a Hamiltonian formulated under the dipole approximation and the rotating-wave approximation, expressed as:

$$\begin{aligned} H = & -\hbar\Delta_p(|c\rangle\langle c| + |b\rangle\langle b|) - \frac{\hbar}{2}\Big(\Omega_p|c\rangle\langle a|e^{-i\phi_p} \\ & + \Omega_c|c\rangle\langle b|e^{-i\phi_c} + \Omega_s|b\rangle\langle a|e^{-i\phi_s} + \text{H.c.}\Big). \end{aligned} \tag{1}$$

In this expression, Ω_c, Ω_p, and Ω_s denote the Rabi frequencies of the cavity, probe, and microwave fields, respectively. The quantities ϕ_c, ϕ_p, and ϕ_s correspond to the global phases of the cavity, probe, and microwave fields. Meanwhile, Δ_p denotes the detuning of the probe field.

The Rabi frequency associated with the cavity mode is expressed as

$$\Omega_c = 2g\sqrt{n+1}, \tag{2}$$

where g is the atom-cavity coupling constant, and n is the number of photons in the cavity. Here, n denotes the intracavity photon number of the quantized cavity mode. In the present model, $n = 0$ corresponds to the vacuum field case, while $n > 0$ is introduced

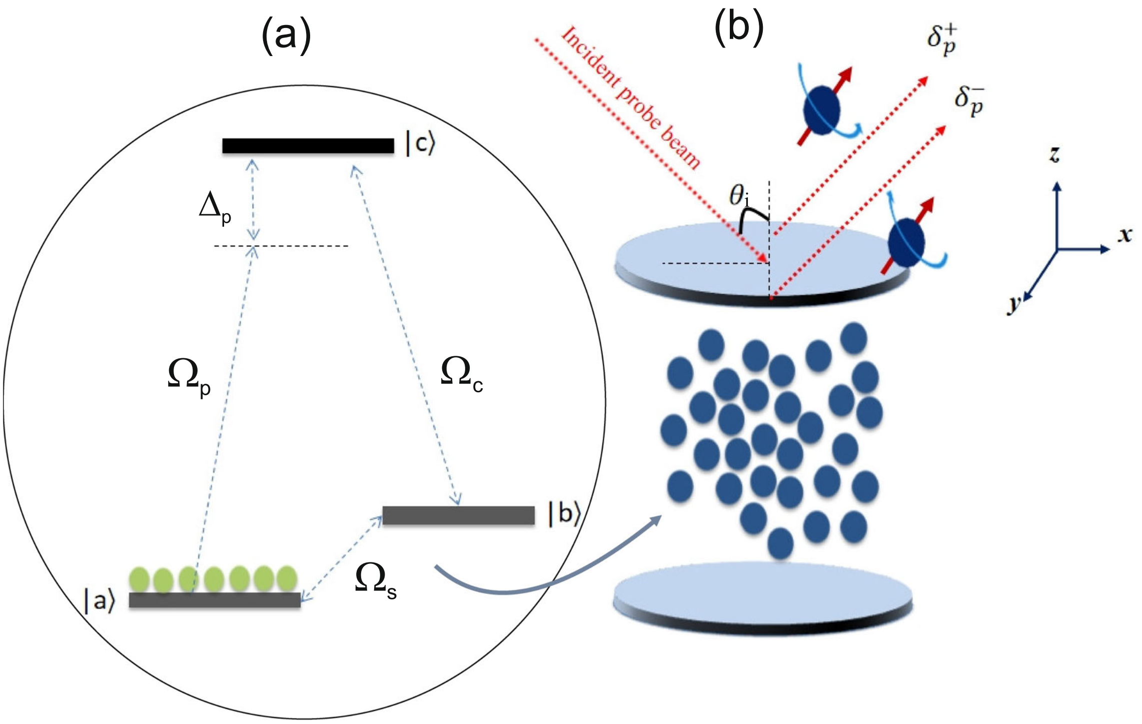

Fig. 1 **a** Schematic representation of a three-layer cavity configuration composed of two mirrors, M_1 and M_2, with a medium of coherently interacting Δ atoms embedded within a structure composed of dielectric slabs. The dielectric constants of the mirrors are $\epsilon_1 = \epsilon_3 = 2.22$, chosen to represent typical high-transparency coatings at 780 nm. When a TM-polarized beam strikes the surface of mirror M_1, the reflected light experiences a spin-dependent separation. **b** Illustration of the three-level atomic system, consisting of an ensemble of three-level atoms coupled to a high-finesse optical cavity and driven by a weak probe laser field

as a finite photon intracavity field scenario to examine how the effective atom–cavity coupling modifies the optical response and the PSHE. The cooperative parameter is defined as:

$$\beta = \frac{4g^2}{\kappa \gamma_{ca}}. \tag{3}$$

Here, κ denotes the cavity decay rate, and γ_{ca} represents the atomic decay rate. A condition of $\beta \gg 1$ corresponds to the strong coupling regime, which occurs when $g > \kappa$ and $g > \gamma_{ca}$. In the present work, the cavity decay rate is taken from the experimental cavity parameters reported in Ref. [3], with $\kappa/2\pi = 173 \pm 13$ kHz, i.e., $\kappa = 2\pi \times (173 \pm 13)$ kHz. For the parameters $g = 0.25\gamma$ and $\gamma_{ca} = 1.25\gamma$, this corresponds to a cooperativity $\beta \approx 0.184$ for $\gamma = 1$ MHz.

To compute the optical susceptibility, we begin by formulating the density matrix equations using:

$$\dot{\rho} = -\frac{i}{\hbar}[H, \rho] - \frac{1}{2}\{\Gamma, \rho\}, \tag{4}$$

where Γ represents the decay matrix. Applying standard approximations and assuming that all atoms are initially in the ground state $|a\rangle$, i.e., $\rho_{aa}^{(0)} = 1$ and $\rho_{cc}^{(0)} = \rho_{bb}^{(0)} = 0$, one obtains

$$\dot{\rho}_{ca} = \frac{i}{2}\left(\Omega_c \rho_{ba} e^{-i\phi_c} + \Omega_p e^{-i\phi_p}\right) + (i\Delta_p - \gamma_{ca})\rho_{ca}, \tag{5}$$

$$\dot{\rho}_{ba} = \frac{i}{2}\left(\Omega_c \rho_{ca} e^{i\phi_c} + \Omega_s e^{-i\phi_s}\right) + (i\Delta_p - \gamma_{ba})\rho_{ba}. \tag{6}$$

Here, γ_{ca} is treated as the bare atomic spontaneous decay rate (equivalently, the Einstein A coefficient for the relevant transition), while γ_{ba} denotes an effective ground-state coherence dephasing rate. In the present model, these decay parameters are assumed to remain fixed, and cavity-induced modifications of spontaneous emission are not included explicitly. Solving these equations in steady state yields

$$\rho_{ca} = \frac{2i\Omega_p \gamma_{ba} + 2\Omega_p \Delta_p - \Omega_c \Omega_s e^{i\phi}}{4(\gamma_{ba} - i\Delta_p)(\gamma_{ca} - i\Delta_p) + \Omega_c^2}, \tag{7}$$

where $\phi = \phi_p - \phi_s - \phi_c$ describes the relative phase.

The optical susceptibility χ is given by:

$$\chi = \frac{N_a|\mu_{ca}|^2}{\hbar\epsilon_0\Omega_p}\rho_{ca}, \tag{8}$$

and hence:

$$\chi = \eta \cdot \frac{2i\gamma_{ba} + 2\Delta_p - \Omega_p^{-1}\Omega_c\Omega_s e^{i\phi}}{4(\gamma_{ba} - i\Delta_p)(\gamma_{ca} - i\Delta_p) + \Omega_c^2}, \tag{9}$$

where $\eta = \frac{N_a|\mu_{ca}|^2}{\hbar\epsilon_0}$.

Here, γ_{ba} represents an effective ground state coherence dephasing rate introduced phenomenologically in normalized units, whereas Doppler broadening is incorporated independently through velocity averaging of the susceptibility.

3 Modeling spin-dependent light deflection

We examine the dynamics of a weak probe beam as it interacts with the cavity–atom system illustrated in Fig. 1(b). The incident probe field contains both TE- and TM-polarized components and strikes mirror M_1 at an angle θ_i, enabling its coupling to the enclosed three-level atomic ensemble. The probe is treated as a monochromatic Gaussian beam that may be either transmitted through or reflected from the medium.

Upon reflection, the left- and right-circular polarization components of the beam undergo lateral shifts of the same magnitude but in opposite directions along the axis perpendicular to the plane of incidence (the y-axis). These contrasting displacements give rise to a vacuum-induced PSHE, as depicted in Fig. 1(b). For the three-layer configuration under consideration, the reflection coefficients for TM polarization, R_M, and TE polarization, R_s, are obtained using the Transfer Matrix Method, leading to

$$R_{p,s} = \frac{R_{12,p,s} + R_{23,p,s}\, e^{2ik_{2z}q}}{1 + R_{12,p,s}R_{23,p,s}\, e^{2ik_{2z}q}}. \tag{10}$$

In this expression, q corresponds to the physical thickness of the intracavity medium. The terms $R_{12,\,p/s}$ and $R_{23,\,p/s}$ correspond to the TM/TE reflection coefficients at the interface between the first mirror along with the atomic medium, and between the atomic medium as well as the second mirror. For a two-layer configuration, the effective TM reflection coefficient for the combined top mirror–medium–bottom mirror interface is expressed as:

$$R_{ij,p} = \frac{\epsilon_j k_{iz} - \epsilon_i k_{jz}}{\epsilon_j k_{iz} + \epsilon_i k_{jz}}. \tag{11}$$

For TE-polarized light, the reflection coefficient can be written as:

$$R_{ij,s} = \frac{k_{iz} - k_{jz}}{k_{iz} + k_{jz}}. \tag{12}$$

In this formulation, the longitudinal wave vector component in each layer is defined as $k_{iz} = \sqrt{k_0^2\epsilon_i - k_x^2}$, where $k_x = \sqrt{\epsilon_1}\, k_0 \sin(\theta_i)$ denotes the component of the wave vector parallel to the x-axis. The parameter $k_0 = 2\pi/\lambda$ represents the free-space wavenumber corresponding to an incident wavelength λ. As shown in Eq. (10), the reflection amplitudes depend on the permittivity of the Δ type atomic medium, ϵ_2. This permittivity is determined by the optical susceptibility χ, enabling active control over the spin-dependent transverse shift of the reflected beam.

For a TM-polarized Gaussian beam striking the interface between two layers, the reflected right- as well as left-circular polarization components are distributed within the reflection system according to:

$$\begin{aligned}\mathcal{E}_r^{\pm}(x_r, y_r, z_r) =& \frac{\omega_0}{\omega}\exp[-\frac{x_r^2 + y_r^2}{\omega}]\times\\ &[R_p - \frac{2ix_r}{k\omega}\frac{\partial R_p}{\partial\theta_i} \mp \frac{2y_r\cot[\theta_i]}{k\omega}\times\\ &(R_s + R_p)],\end{aligned} \tag{13}$$

where $\omega = \omega_0\big[1 + (2z_r/k_1\omega_0^2)^2\big]^{1/2}$, and $z_r = k_1\omega_0^2/2$ denotes the Rayleigh range. The parameter ω_0 represents the waist radius of the incident Gaussian beam, while $(x_r,\ y_r,\ z_r)$ defines the coordinate system associated with the reflected field. The ± signs correspond to the two opposite spin components. In the geometry of the present cavity, the PSHE is most strongly enhanced for TM-polarized incidence because the p-polarized reflection coefficient exhibits a pronounced angular variation near the Brewster region. Although an analogous treatment for the TE-polarized incidence can be written formally, the resulting transverse spin shift is much weaker in this configuration and is therefore not considered here.

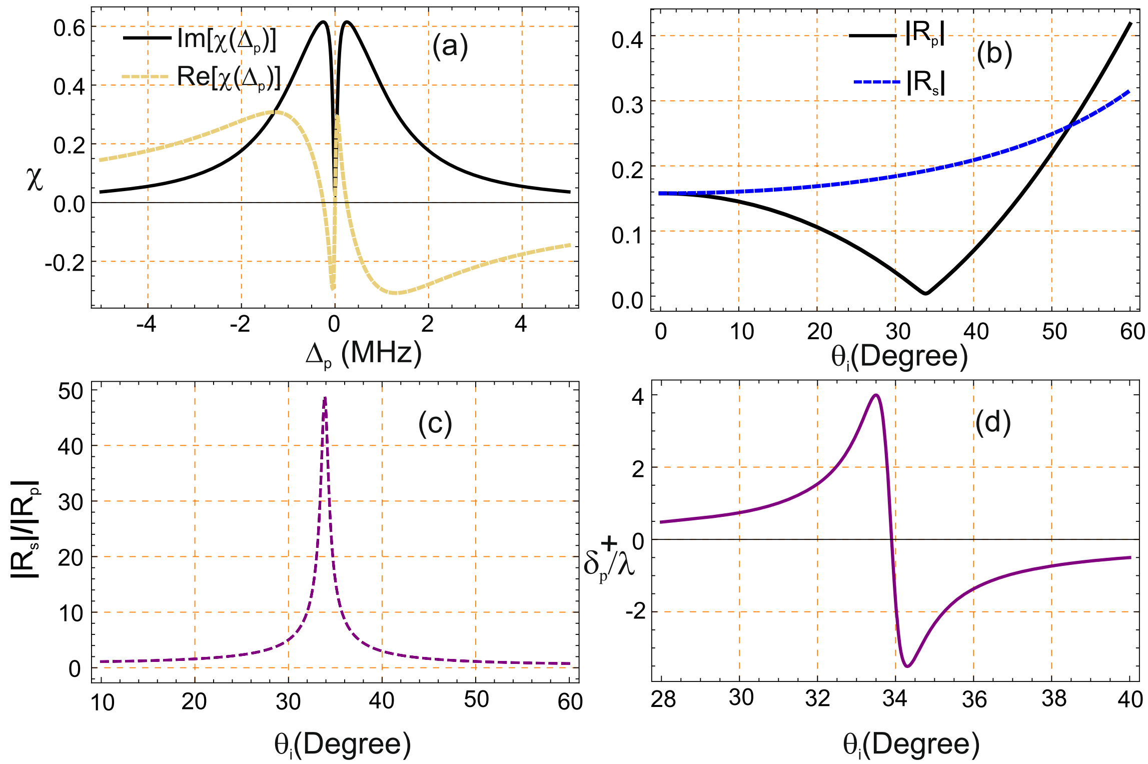

Fig. 2 **a** Absorptive (solid line) and dispersive (dashed line) parts of the cavity-induced susceptibility for a single atom plotted against the normalized probe detuning Δ_p/γ. **b** Fresnel reflection amplitudes $|R_s|$ and $|R_p|$ as functions of the incident angle θ_i. **c** Angular dependence of the ratio $|R_s|/|R_p|$. **d** Transverse photonic spin Hall shift δ_p^+ versus θ_i. A reversal in the sign of the PSHE when the ratio $|R_s|/|R_p|$ reaches its peak. Panels (b)–(d) are evaluated at a fixed probe detuning $\Delta_p = 0$. The parameters employed in the calculations are: $\gamma = 1$MHz, $\gamma_{ba} = 0.0025\gamma$, $\gamma_{ca} = 1.25\gamma$, $\Omega_p = 0.6\gamma$, $g = 0.25\gamma$, $\mathcal{N}/V = 1.8\times10^{12}$ m^{-3}, $\Omega_c = 2g\sqrt{n+1}$, $n = 0$, $\Omega_s = 0$, $\phi = \pi/2$, $\epsilon_0 = 8.85\times10^{-12}$ F/m, $\hbar = 1.05\times10^{-34}$ J·s, $e = 1.6\times10^{-19}$ C, $a_0 = 0.5\times10^{-10}$ m, $\mu = 3.5247\, e\, a_0$, wavelength $\lambda = 780$ nm, free-space wave number $k_0 = 2\pi/\lambda$, beam waist $\omega_0 = 30\lambda$, Gaussian beam parameter $q = 0.05\times10^{-6}$ m, and dielectric constants $\epsilon_1 = \epsilon_3 = 2.22$, $\epsilon_2 = 1+\chi$

Under these conditions, the transverse shift experienced by the reflected beam can be written as

$$\delta_p^{\pm} = \frac{\int y|\mathcal{E}_r^{\pm}(x_r, y_r, z_r)|^2 dx_r dy_r}{\int|\mathcal{E}_r^{\pm}(x_r, y_r, z_r)|^2 dx_r dy_r}. \tag{14}$$

By combining Eq. (13) as well as Eq. (14), the transverse spin displacement components, δ_p^+ and δ_p^-, can be expressed in terms of the reflection coefficients of the three-layer cavity system [35, 36]

$$\delta_p^{\pm} = \mp\frac{k_1\omega_0^2\,\mathrm{Re}\left[1+\frac{R_s}{R_p}\right]\cot\theta_i}{k_1^2\omega_0^2 + \left|\frac{\partial \ln R_p}{\partial\theta_i}\right|^2 + \left|\left(1+\frac{R_s}{R_p}\right)\cot\theta_i\right|^2}. \tag{15}$$

In Eq. (15), $\delta_p^{\pm}$ denotes the transverse separation between the left- and right-circularly polarized components of the incident beam, with $k_1 = \sqrt{\epsilon_1}k$. In the analysis that follows, we focus on the transverse displacement δ_p^+ corresponding to the left circularly polarized component. Since the two spin states exhibit shifts of identical magnitude but opposite direction, the behavior of the right circularly polarized component can be tuned in an analogous way.

Furthermore, the outer dielectric media are taken as $\epsilon_1 = \epsilon_3 = 2.22$ ($n \approx 1.49$), corresponding to optically transparent materials such as BK7 glass or fused silica at 780 nm. Adopting equal permittivities on both sides preserves the symmetry of the cavity boundaries and simplifies the treatment of the spin-dependent transverse shifts. In contrast, if $\epsilon_1 \neq \epsilon_3$, the reflection coefficients R_p and R_s become asymmetric, leading to quantitative changes in the magnitude and angular position of the PSHE without affecting its basic physical mechanism. The intracavity medium is characterized separately by $\epsilon_2 = 1+\chi$, where χ denotes the susceptibility of the Δ-type atomic ensemble, as given in Eq. (9).

it should be pointed out that in principle, an air-medium case (e.g., $\epsilon_1 = 1$ or $\epsilon_3 = 1$) can also be analyzed within the same formalism; however, the reduced dielectric contrast would yield a weaker quantitative response.

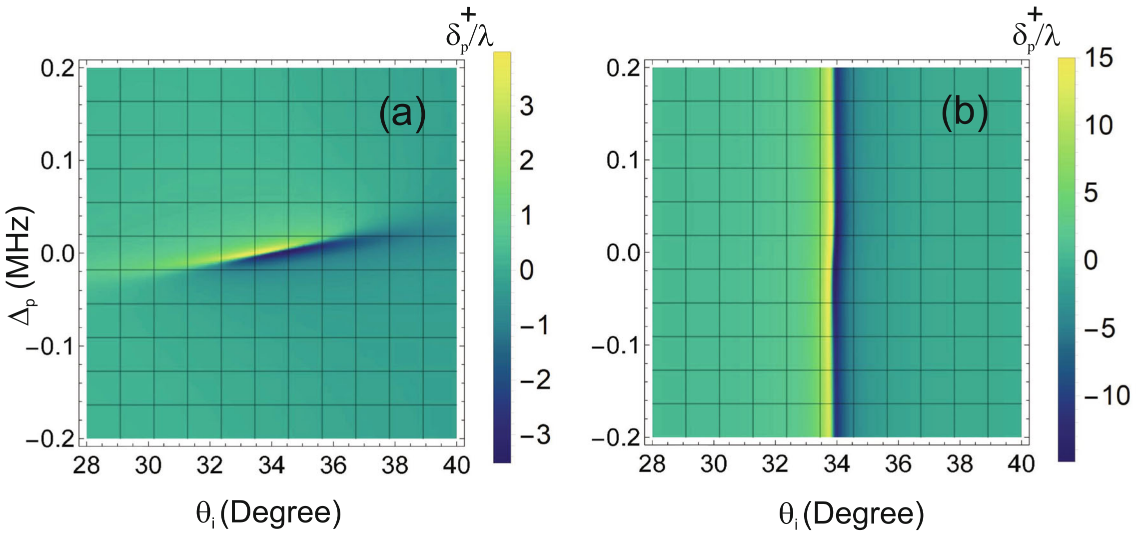

Fig. 3 **a** Density map of the PSHE displacement δ_p^+ as a function of probe detuning Δ_p/γ and incidence angle θ_i for an atomic number density of $\mathcal{N}/V = 1.8 \times 10^{12}$ m^{-3}. **b** Corresponding density plot of δ_p^+ for a reduced atomic density, decreased by one order of magnitude to $\mathcal{N}/V = 1.8 \times 10^{10}$ m^{-3}. Parameters used: $\gamma = 1$MHz, $\gamma_{ba} = 0.0025\gamma$, $\gamma_{ca} = 1.25\gamma$, $\Omega_p = 0.6\gamma$, $g = 0.25\gamma$, $\Omega_c = 2g\sqrt{n+1}$, $n = 0$, $\Omega_s = 0$, $\phi = \pi/2$, $\epsilon_0 = 8.85 \times 10^{-12}$ F/m, $\hbar = 1.05 \times 10^{-34}$ J·s, $e = 1.6 \times 10^{-19}$ C, $a_0 = 0.5 \times 10^{-10}$ m, $\mu = 3.5247\, e\, a_0$, wavelength $\lambda = 780$ nm, free-space wavenumber $k_0 = 2\pi/\lambda$, beam waist $\omega_0 = 30\lambda$, Gaussian beam parameter $q = 0.05 \times 10^{-6}$ m, and dielectric constants $\epsilon_1 = \epsilon_3 = 2.22$, $\epsilon_2 = 1 + \chi$

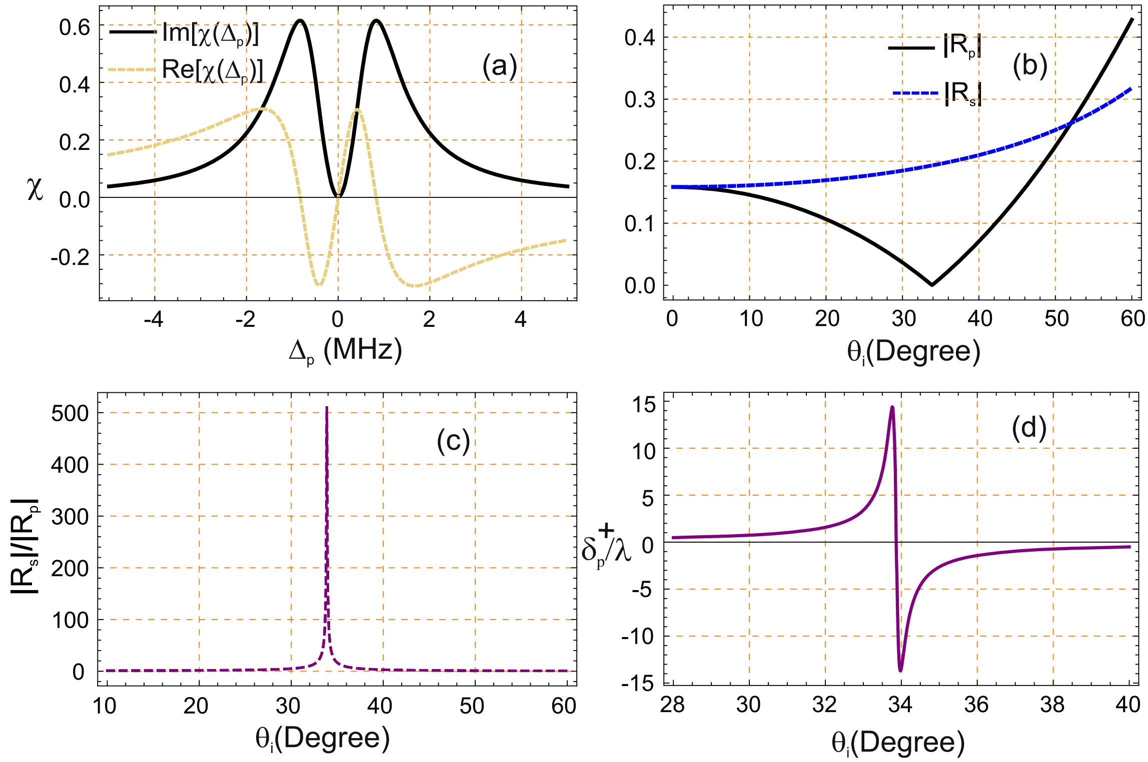

Fig. 4 **a** Absorption (solid line) and dispersion (dashed line) characteristics of the cavity susceptibility for a single atom as functions of normalized probe detuning Δ_p/γ. **b** Fresnel reflection coefficients $|R_s|$ and $|R_p|$ as functions of the incidence angle θ_i. **c** Ratio $|R_s|/|R_p|$ plotted against θ_i. **d** PSHE displacement δ_p^+ versus θ_i. In Fig. (b)–(d), the probe detuning is fixed at $\Delta_p = 0$. Additional parameters used throughout: $\gamma = 1$MHz, $\gamma_{ba} = 0.0025\gamma$, $\gamma_{ca} = 1.25\Gamma$, $\Omega_p = 0.6\gamma$, $g = 0.25\gamma$, $\mathcal{N}/V = 1.8 \times 10^{12} m^{-3}$, $\Omega_c = 2g\sqrt{n+1}$, $n = 10$, $\Omega_s = 0$, $\phi = \pi/2$, $\epsilon_0 = 8.85 \times 10^{-12}$ F/m, $\hbar = 1.05 \times 10^{-34}$ J·s, $e = 1.6 \times 10^{-19}$ C, $a_0 = 0.5 \times 10^{-10}$ m, $\mu = 3.5247\, e\, a_0$, wavelength $\lambda = 780$ nm, free-space wave vector $k_0 = 2\pi/\lambda$, beam waist $\omega_0 = 30\lambda$, Gaussian beam shift parameter $q = 0.05 \times 10^{-6}$ m, and permittivities $\epsilon_1 = \epsilon_3 = 2.22$, $\epsilon_2 = 1 + \chi$

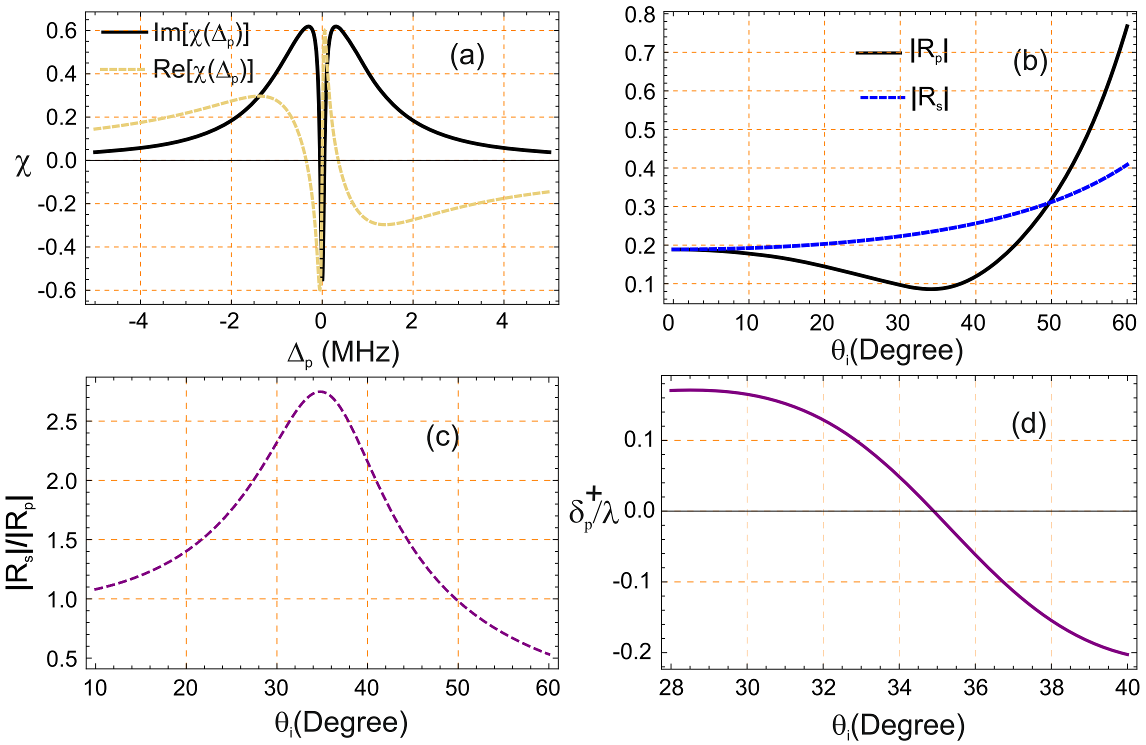

Fig. 5 **a** Absorptive (solid line) and dispersive (dashed line) parts of the cavity-induced susceptibility for a single atom plotted as functions of the normalized probe detuning Δ_p/γ. **b** Fresnel reflection amplitudes $|R_s|$ and $|R_p|$ as a function of the incidence angle θ_i. **c** The ratio $|R_s|/|R_p|$ displayed as a function of θ_i. **d** Corresponding PSHE-induced transverse shift δ_p^+ versus θ_i. For panels (b)–(d), the probe detuning is fixed at $\Delta_p = 0$. The parameters used throughout the figure are: $\gamma = 1\text{MHz}$, $\gamma_{ba} = 0.0025\gamma$, $\gamma_{ca} = 1.25\gamma$, $\Omega_p = 0.6\gamma$, $g = 0.25\gamma$, $\mathcal{N}/V = 1.8 \times 10^{12}\,\text{m}^{-3}$, $\Omega_c = 2g\sqrt{n+1}$ with $n = 0$, $\Omega_s = 0.12\gamma$, $\phi = \pi/2$, $\epsilon_0 = 8.85 \times 10^{-12}\,\text{F/m}$, $\hbar = 1.05 \times 10^{-34}\,\text{J} \cdot \text{s}$, $e = 1.6 \times 10^{-19}\,\text{C}$, $a_0 = 0.5 \times 10^{-10}\,\text{m}$, $\mu = 3.5247\, e\, a_0$, wavelength $\lambda = 780\,\text{nm}$, free-space wave vector $k_0 = 2\pi/\lambda$, beam waist $\omega_0 = 30\lambda$, Gaussian shift parameter $q = 0.05 \times 10^{-6}\,\text{m}$, and dielectric constants $\epsilon_1 = \epsilon_3 = 2.22$, $\epsilon_2 = 1 + \chi$

4 Results

Figure 2 presents a detailed analysis of the optical response and spin-dependent light-matter interaction in the proposed atomic system. Fig. 2(a) displays the real and imaginary parts of the cavity-modified atomic susceptibility $\chi(\Delta_p)$ as functions of the normalized probe detuning Δ_p/γ. The imaginary part, $\text{Im}[\chi(\Delta_p)]$ (solid curve), exhibits a distinct transparency window centered at $\Delta_p = 0$, which originates from *vacuum-induced transparency* (VIT). This phenomenon arises even in the absence of photons in the control field (i.e., $n = 0$), due to quantum vacuum fluctuations mediating the atom-cavity interaction—resulting in a nonzero vacuum Rabi coupling. Conversely, the real part, $\text{Re}[\chi(\Delta_p)]$ (dashed curve), reveals a sharp dispersive slope near resonance, which plays a critical role in facilitating strong spin–orbit interaction and enhancing the PSHE.

Fig. 2(b) illustrates the Fresnel reflection coefficients $|R_p|$ and $|R_s|$ for p- and s-polarized components of the reflected probe, plotted as functions of the incidence angle θ_i. The p-polarized reflection coefficient $|R_p|$ shows a minimum near the Brewster angle, indicating near-complete transmission of p-polarized light, while $|R_s|$ increases steadily with θ_i. This anisotropic reflection is fundamental to inducing polarization-dependent interactions, which are necessary for the manifestation of the PSHE.

In Fig. 2(c), the ratio $|R_s|/|R_p|$ is plotted against θ_i, exhibiting a sharp peak around the Brewster angle. This peak reflects the angular region where polarization contrast is maximized, leading to enhanced spin-dependent splitting. The prominence of this feature marks the optimal regime for spin–orbit interaction–induced PSHE.

Figure 2(d) shows the vacuum-induced spin Hall displacement δ_p^+ of the reflected probe beam, normalized by the probe wavelength λ, as a function of θ_i. The displacement undergoes a sign reversal near the Brewster angle, aligning with the maximum in the $|R_s|/|R_p|$ ratio seen in Fig. 2(c). This reversal underscores the topological characteristics of spin–orbit coupling and corresponds to spin-dependent transverse momentum shifts of the reflected light. The largest values of δ_p^+ occur under conditions of strongest polarization anisotropy, highlighting the importance of angle tuning in controlling spin-dependent optical effects.

Here we would like to mention that in Fig. 2(b)–(d), the probe detuning is fixed at $\Delta_p = 0$, and the system operates under the following conditions: $\Omega_c = 2g\sqrt{n+1}$ with $n = 0$ (i.e., the control field is in the vacuum state), $\Omega_s = 0$ (no microwave coupling), $\gamma_{ca} = 1.25\gamma$, and dielectric constants $\epsilon_1 = \epsilon_3 = 2.22$. These parameters place the system firmly in the vacuum field regime, demonstrating that the observed transparency and associated spin-dependent effects stem entirely from vacuum fluctuations, i.e.,

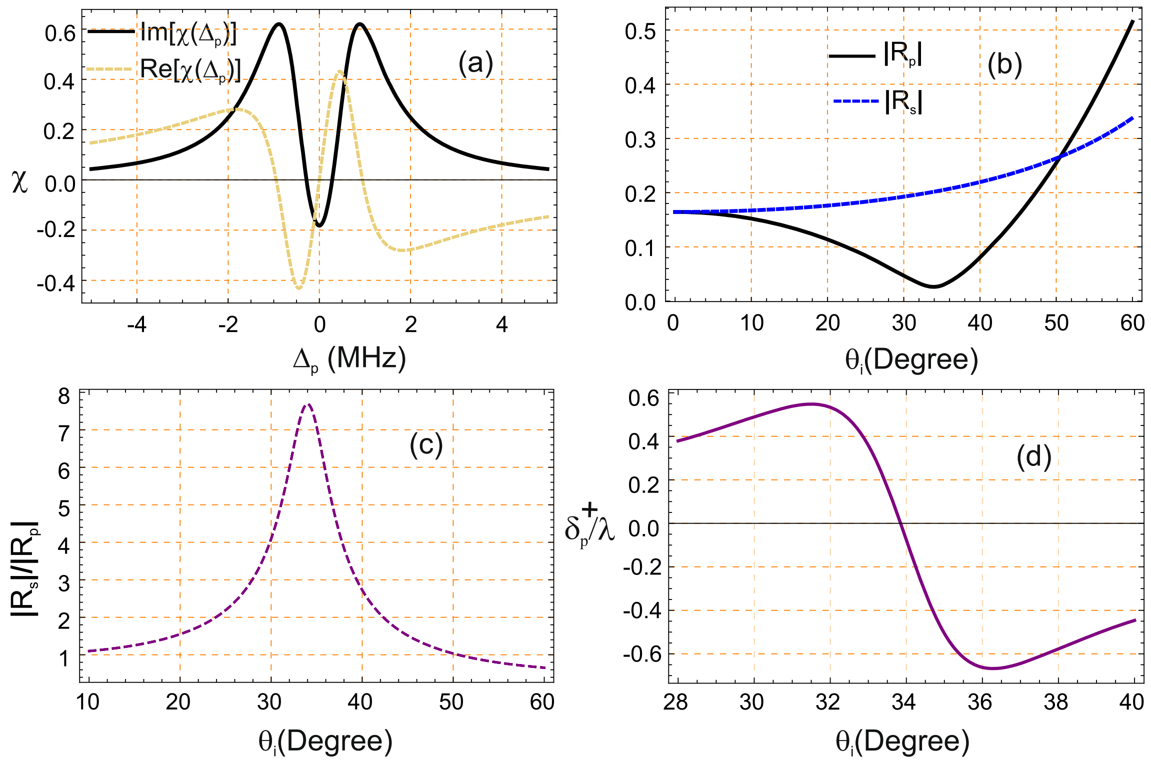

Fig. 6 **a** Absorption spectrum (solid line) and dispersion spectrum (dashed line) of the cavity susceptibility for a single atom as a function of normalized probe detuning Δ_p/γ. **b** Fresnel reflection amplitudes $|R_s|$ and $|R_p|$ as functions of the incidence angle θ_i. **c** The ratio $|R_s|/|R_p|$ plotted against θ_i. **d** PSHE displacement δ_p^+ versus θ_i, where the sign reversal occurs close to the incidence angle corresponding to the peak of $|R_s|/|R_p|$. For Fig. (b)–(d), the probe detuning is kept at $\Delta_p = 0$. Additional parameters used throughout: $\gamma = 1\text{MHz}, \gamma_{ba} = 0.0025\gamma, \gamma_{ca} = 1.25\gamma, \Omega_p = 0.6\gamma, g = 0.25\gamma, \mathcal{N}/V = 1.8\times10^{12}$, $\Omega_c = 2g\sqrt{n+1}, n = 10, \Omega_s = 0.12\gamma, \phi = \pi/2, \epsilon_0 = 8.85\times10^{-12}$ F/m, $\hbar = 1.05\times10^{-34}$ J·s, $e = 1.6\times10^{-19}$ C, $a_0 = 0.5\times10^{-10}$ m, $\mu = 3.5247\,e\,a_0$, wavelength $\lambda = 780$ nm, free-space wave vector $k_0 = 2\pi/\lambda$, beam waist $\omega_0 = 30\lambda$, Gaussian beam shift parameter $q = 0.05\times10^{-6}$ m, and permittivities $\epsilon_1 = \epsilon_3 = 2.22, \epsilon_2 = 1+\chi$

vacuum-induced transparency without any classical control field. This configuration allows for a clear investigation of how incidence angle and polarization anisotropy govern the photonic spin shift in a quantum optical setting.

Figure 3 shows a comparative density map of the PSHE-induced shift δ_p^+ plotted as a function of the incident angle θ_i and the normalized probe detuning Δ_p/γ, evaluated for two different atomic number densities. The system parameters are identical to those used in Fig. 2; in particular, $\Omega_c = 2g\sqrt{n+1}$ with $n = 0$ (corresponding to a vacuum control field), $\Omega_s = 0$ (no microwave coupling), $\gamma_{ca} = 1.25\gamma$, and permittivities $\epsilon_1 = \epsilon_3 = 2.22$, placing the configuration firmly within the VIT regime. As illustrated in Fig. 3(a), when the atomic number density is relatively high, $N/V = 1.8\times10^{12}\ \text{m}^{-3}$, the transverse shift δ_p^+ shows a strong sensitivity to variations in the probe detuning Δ_p. A pronounced enhancement is observed near the Brewster angle ($\theta_i \approx 33.8°$), and the displacement exhibits sharp resonance features for small changes in Δ_p. This behavior reflects the enhanced light–matter interaction in a dense atomic medium. Consequently, the spin–orbit interaction becomes highly sensitive to spectral tuning of the probe field, generating a strongly detuning-dependent PSHE signature.

In contrast, Fig. 3(b) depicts the behavior of the system at a lower atomic density of $N/V = 1.8\times10^{11}\ \text{m}^{-3}$. In this dilute limit, the PSHE displacement δ_p^+ shows a minimal dependence on Δ_p, as reflected by the nearly uniform and vertical color bands along the detuning axis. The suppression of detuning dependence suggests the diminishing role of collective interactions, with the system behaving more like an ensemble of noninteracting atoms. Here, the PSHE is predominantly governed by interface geometry and reflection properties rather than medium-induced dispersion. This comparison highlights the critical influence of atomic density in shaping spin-dependent light-matter interactions under vacuum field conditions. While high-density media enable frequency sensitive manipulation of the PSHE via enhanced dispersion effects, low-density systems provide stable and robust control through geometric tuning. This tunable density regime, explored entirely under vacuum-induced transparency conditions, offers a powerful platform for applications in spin-based photonic routing and quantum optical information processing.

Figure 4 illustrates the optical response and PSHE in an atomic system under different photon number regimes of the control field, specifically contrasting the vacuum field case ($n = 0$) with a finite-photon scenario ($n = 10$).

When the number of photons in the control field is increased to $n = 10$, the effective Rabi frequency increases to $\Omega_c = 2g\sqrt{11}$, enhancing the atom-field coupling strength. As a result, the transparency window in the absorption profile broadens, and the dispersion becomes less steep but extends over a wider frequency range. This is evident in Fig. 4(a), where the imaginary part of

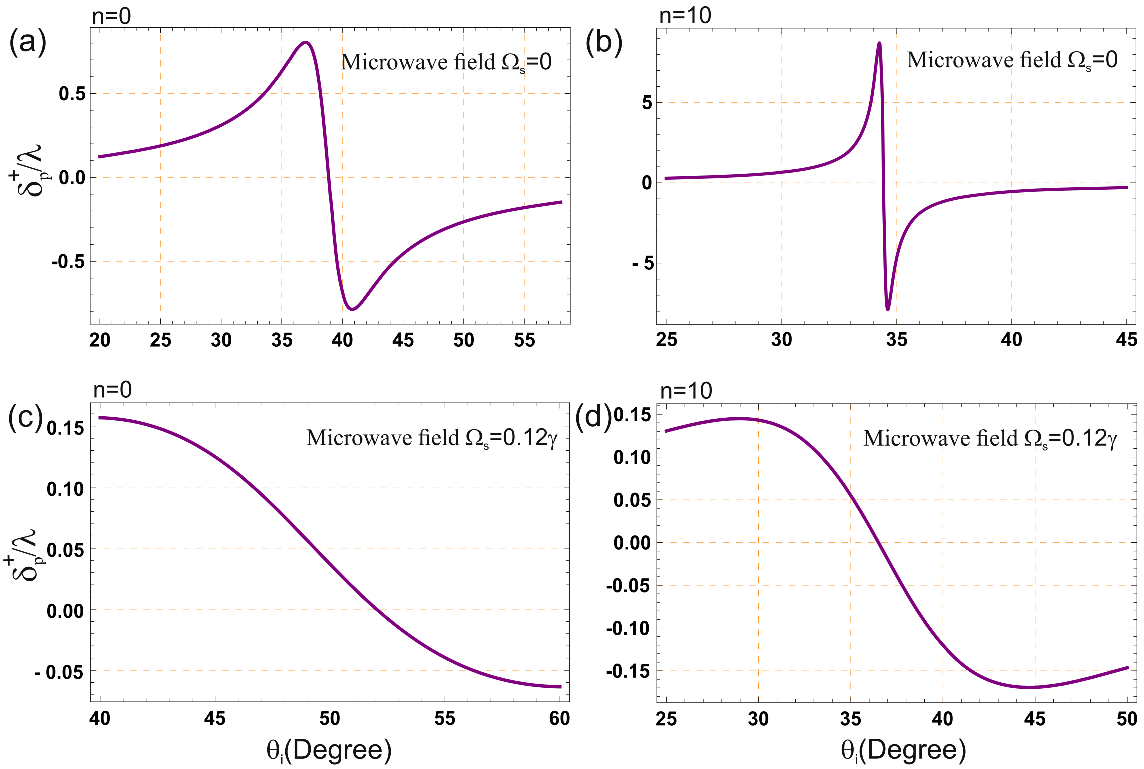

Fig. 7 Transverse PSHE shift δ_p^+ as a function of the incidence angle θ_i in the presence of Doppler broadening. **a** Absence of the microwave drive, $\Omega_s = 0$, with cavity photon number $n = 0$; **b** Same conditions as in (a) but with $n = 10$; **c** Weak microwave coupling applied, $\Omega_s = 0.12\gamma$, with $n = 0$; **d** Microwave field applied, $\Omega_s = 0.12\gamma$, and $n = 10$. In all cases, the PSHE exhibits a characteristic sign change near the angle at which the polarization contrast ratio $|R_s|/|R_p|$ reaches its maximum. Panels (a)–(d) are evaluated at a fixed probe detuning of $\Delta_p = 0$. The parameters used throughout the figure are: $\gamma = 1\text{MHz}$, $\gamma_{ab} = 0.0025\gamma$, $\gamma_{ca} = 1.25\gamma$, $\Omega_p = 0.6\gamma$, $g = 0.25\gamma$, $\mathcal{N}/V = 1.8 \times 10^{12}\,\text{m}^{-3}$, $\Omega_c = 2g\sqrt{n+1}$, $\phi = \pi/2$, $\epsilon_0 = 8.85 \times 10^{-12}\,\text{F/m}$, $\hbar = 1.05 \times 10^{-34}\,\text{J}\cdot\text{s}$, $e = 1.6 \times 10^{-19}\,\text{C}$, $a_0 = 0.5 \times 10^{-10}\,\text{m}$, $\mu = 3.5247\, e\, a_0$, wavelength $\lambda = 780\,\text{nm}$, free-space wavenumber $k_0 = 2\pi/\lambda$, beam waist $\omega_0 = 30\lambda$, Gaussian parameter $q = 0.05 \times 10^{-6}\,\text{m}$, and dielectric constants $\epsilon_1 = \epsilon_3 = 2.22$, $\epsilon_2 = 1 + \chi^{\text{DB}}$

the susceptibility shows a significantly broadened transparency dip, and the real part evolves accordingly, reflecting the stronger, photon number-enhanced coupling.

Figure 4(b)–(d) shows the corresponding reflection and PSHE behavior. In Fig. 4(b), the Fresnel reflection coefficients $|R_s|$ and $|R_p|$ exhibit subtle changes compared to the vacuum case, with slightly sharper features near the Brewster angle ($\theta_i \approx 33.8°$) due to modified susceptibility profiles. The ratio $|R_s|/|R_p|$, plotted in Fig. 4(c), becomes more pronounced, highlighting enhanced polarization anisotropy induced by the stronger atom-field interaction at $n = 10$.

Finally, Fig. 4(d) displays the PSHE displacement δ_p^+ as a function of incidence angle. Compared to the $n = 0$ case, the displacement increases in magnitude and becomes more sensitive to angular variations. The maximal displacement occurs near the Brewster angle, where the optical anisotropy is strongest, reaching several wavelengths. The enhanced spin-dependent splitting reflects the increased optical nonlinearity introduced by the presence of photons in the control field.

Therefore, transitioning from $n = 0$ (vacuum control field) to $n = 10$ (finite intracavity photon number) moves the system from the vacuum-induced regime to a non-vacuum finite-photon regime with stronger effective atom–cavity coupling. This leads to broader transparency windows and an enhanced PSHE response, providing tunable control of light–matter interactions through the intracavity photon occupation.

Here we note that in Figures (2-4), the microwave field is absent ($\Omega_s = 0$). Under these conditions, the relative phase $\phi = \phi_p - \phi_s - \phi_c$ does not influence the dynamics and is therefore irrelevant for the system evolution. For consistency in plotting, ϕ is retained at $\pi/2$, but it does not affect the observed PSHE displacement. All other parameters remain unchanged: $\Omega_c = 2g\sqrt{n+1}$ with $n = 0$, $\gamma_{ca} = 1.25\gamma$, and dielectric constants $\epsilon_1 = \epsilon_3 = 2.22$.

Figure 5 investigates the vacuum-induced PSHE and optical response of a atom-cavity system interacting with a vacuum control field ($n = 0$) and a weak microwave field $\Omega_s \neq 0$. This configuration corresponds to the regime of VIT modified by coherent microwave driving, which significantly alters both the linear susceptibility and spin-dependent beam shifts. The impact of microwave-induced gain on the transparency window and its consequences for the PSHE are analyzed in detail below.

Fig. 5(a) displays the absorption (solid curve) and dispersion (dashed curve) profiles of the cavity-modified atomic susceptibility $\chi(\Delta_p)$ as functions of normalized probe detuning Δ_p/γ. Due to the vacuum field ($n = 0$), the transparency window at $\Delta_p = 0$

originates from VIT, where destructive quantum interference prevents absorption even in the absence of photons in the control mode. The addition of a nonzero microwave field $\Omega_s = 0.12\gamma$ couples the ground states and introduces population redistribution, which leads to gain within the transparency window. As a result, the imaginary part $\mathrm{Im}[\chi(\Delta_p)]$ dips below zero at resonance, indicating amplification. Simultaneously, the real part $\mathrm{Re}[\chi(\Delta_p)]$ exhibits a steep normal dispersion around $\Delta_p = 0$, which is a prerequisite for strong spin–orbit coupling in PSHE.

However, the presence of gain window modifies the nature of light-matter interaction in a critical way. In particular, gain reduces the effective refractive index contrast and modifies the boundary conditions for the reflected probe beam. This results in a suppression of the PSHE, as discussed below.

Fig. 5(b) presents the Fresnel reflection coefficients $|R_s|$ and $|R_p|$ for *s*- and *p*-polarized components, respectively, as functions of incidence angle θ_i. The coefficient $|R_p|$ reaches a minimum near the Brewster angle ($\theta_i \approx 33.8°$), where *p*-polarized light undergoes near-complete transmission. Meanwhile, $|R_s|$ increases monotonically, giving rise to polarization asymmetry necessary for spin-dependent beam shifts. The ratio $|R_s|/|R_p|$, plotted in Fig. 5(c), exhibits a peak close to the Brewster angle. This ratio governs the magnitude and sign of the transverse spin splitting due to the PSHE. As in previous figures, this peak denotes the regime where polarization contrast is maximized, enhancing angular sensitivity to the spin degree of freedom.

Despite the favorable dispersion conditions, the actual PSHE displacement δ_p^+ shown in Fig. 5(d) is relatively small in magnitude. The displacement undergoes a sign reversal around the Brewster angle, consistent with the peak of $|R_s|/|R_p|$, but its amplitude remains suppressed compared to configurations without gain. This reduced spin splitting is attributed to the presence of gain in the corresponding window, which effectively flattens the refractive index gradient experienced by the circular polarization components. In particular, the gain compensates for absorption but also diminishes the anisotropy required for a strong spin–orbit interaction. As a result, although steep dispersion is present, the interference pattern responsible for transverse beam splitting is weakened.

This behavior emphasizes an important insight, i.e., steep dispersion alone is not sufficient for strong PSHE. Instead, the interplay between absorption (gain), dispersion, and boundary conditions must be delicately balanced. In this scenario, the gain introduces additional symmetry and reduces the contrast between the reflected spin components, thereby weakening the net spin-dependent displacement. Thus, Figure 5 demonstrates that microwave-assisted vacuum-induced transparency enables narrow windows with gain and steep dispersion. However, the associated gain can suppress the PSHE due to a reduction in polarization-dependent scattering asymmetry. This highlights a subtle tradeoff in spin-optical control: gain can improve transmission and dispersion but at the expense of transverse spin resolution.

The behavior of the system when the number of photons in the control field is set to $n = 10$ is displayed in Figure 6. Compared to Figure 5, where $n = 0$, the most significant difference lies in the enhanced vacuum-induced coupling strength via the control Rabi frequency $\Omega_c = 2g\sqrt{n+1}$. This leads to several notable modifications in both the optical response and the spin–orbit interaction of light.

In Fig. 6(a), the susceptibility profile of a single atom shows a broader window in both absorption (solid curve) and dispersion (dashed curve) compared to the $n = 0$ case. Despite this broadening, the system still exhibits gain around resonance due to the presence of the microwave field $\Omega_s = 0.12\gamma$. The gain is slightly reduced compared to $n = 0$, and more uniformly distributed across the broader transparency region.

Fig. 6(b) and Fig. 6(c) show the Fresnel reflection coefficients $|R_s|$, $|R_p|$, and their ratio $|R_s|/|R_p|$ as functions of the incidence angle θ_i. In the $n = 10$ case, the ratio $|R_s|/|R_p|$ is modestly higher than in the $n = 0$ scenario of Fig. 5, due to the reduced influence of narrowband gain. However, it remains significantly lower than in the absence of gain. The gain modifies the complex refractive index anisotropically, which affects the polarization-selective reflectivity of the interface.

Figure 6(d) illustrates the PSHE displacement δ_p^+ versus the incidence angle θ_i. The PSHE in the $n = 10$ case shows a larger absolute amplitude compared to the $n = 0$ case, indicating stronger light-matter interaction owing to increased control field strength. However, the PSHE remains less sensitive and broader in angle due to the gain-induced suppression of phase anisotropy between *s*- and *p*-polarized components.

The comparison between Figures 5 ($n = 0$) and 6 ($n = 10$) highlights the following trends. Firstly, the amplification window becomes broader with increasing n due to stronger control field coupling. Secondly, gain persists in both cases due to the microwave field, but becomes less dominant for $n = 10$. Thirdly, the ratio $|R_s|/|R_p|$ increases slightly in the $n = 10$ case, improving conditions for PSHE. Fourthly, the PSHE displacement has a larger amplitude at $n = 10$ but is less sharply peaked, indicating a reduced sensitivity to incidence angle.

Overall, while the PSHE weakens in terms of angular selectivity due to gain, increasing the control field photon number compensates by enhancing the strength of the spin-dependent light shift. This interplay enables tunable PSHE characteristics via cavity photon control.

5 Effect of doppler broadening

Up to this point, our analysis of the PSHE has been carried out for a cold atomic ensemble, where atoms are treated as effectively motionless. In realistic experimental scenarios, however, room-temperature operation is often required, and the thermal motion of atoms can no longer be neglected. As the temperature rises, atoms gain kinetic energy and move with higher velocities, leading to

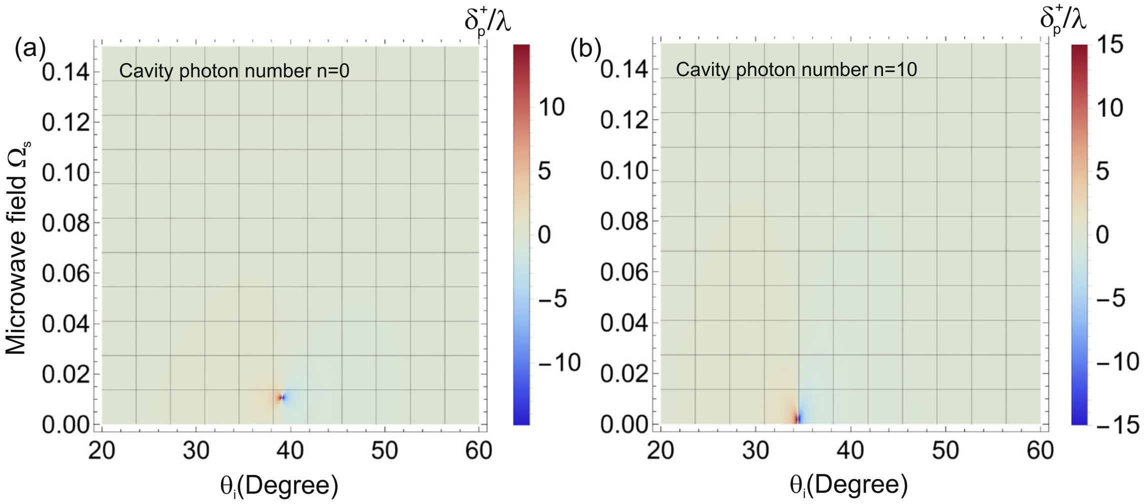

Fig. 8 Density plot of PSHE shift δ_p/λ versus incident angle θ_i and microwave Rabi frequency Ω_s in the presence of Doppler broadening when **a** Cavity photon number, $n = 0$; **b** Cavity photon number, $n = 10$. The parameters used throughout the figure are: $\gamma = 1\text{MHz}$, $\gamma_{ab} = 0.0025\gamma$, $\gamma_{ca} = 1.25\gamma$, $\Omega_p = 0.6\gamma$, $g = 0.25\gamma$, $\mathcal{N}/V = 1.8 \times 10^{12}\,\text{m}^{-3}$, $\Omega_c = 2g\sqrt{n+1}$, $\phi = \pi/2$, $\epsilon_0 = 8.85 \times 10^{-12}\,\text{F/m}$, $\hbar = 1.05 \times 10^{-34}\,\text{J}\cdot\text{s}$, $e = 1.6 \times 10^{-19}\,\text{C}$, $a_0 = 0.5 \times 10^{-10}\,\text{m}$, $\mu = 3.5247\,e\,a_0$, wavelength $\lambda = 780\,\text{nm}$, free-space wavenumber $k_0 = 2\pi/\lambda$, beam waist $\omega_0 = 30\lambda$, Gaussian parameter $q = 0.05 \times 10^{-6}\,\text{m}$, and dielectric constants $\epsilon_1 = \epsilon_3 = 2.22$, $\epsilon_2 = 1 + \chi^{\text{DB}}$

Doppler broadening (DB) in both the absorption and dispersion profiles of the medium. Changes in temperature and the associated DB can significantly influence the optical properties of the intracavity system [37, 38]. It is therefore crucial to investigate how the PSHE behaves in a thermally active medium and to assess the role of DB within the theoretical model.

To analyze the influence of DB on the PSHE shift, we consider a three-level atomic configuration driven by a microwave field. When light interacts with thermally moving atoms, the frequency perceived by each atom experiences a small Doppler-induced shift determined by the component of atomic velocity along the propagation direction. The distribution of atomic velocities inside the cavity follows Maxwell–Boltzmann statistics [39], providing the thermal velocity profile that must be incorporated into the optical response. The resulting modification of the atomic susceptibility in a Doppler-broadened medium has been widely studied in coherent atomic systems [40]. This interaction modifies the susceptibility of the medium such that the probe detuning is effectively transformed according to $\Delta_p \to \Delta_p - k_p v$ in the expression for χ, as indicated in Eqs. (9).

The Doppler-averaged optical susceptibility, denoted by χ^{DB}, is defined as

$$\chi^{\text{DB}} = \langle \chi \rangle_v, \tag{16}$$

where the velocity-averaged susceptibility is obtained from

$$\langle \chi \rangle_v = \frac{1}{\sqrt{2\pi}\,D} \int \chi(\Delta_p - k_p v)\, e^{-v^2/(2D^2)}\, dv. \tag{17}$$

Here, D is the Doppler width associated with the thermal velocity distribution and is given by

$$D = \sqrt{\frac{2k_p^2 k_b T}{M}}. \tag{18}$$

In this expression, M denotes the atomic mass, k_b is the Boltzmann constant, and T is the absolute temperature. The Doppler-broadened permittivity of the intracavity medium therefore becomes $\epsilon_2 = 1 + \chi^{\text{DB}}$. In the present treatment, Doppler broadening is incorporated only through the probe detuning, since the PSHE is evaluated from the reflected probe field, whereas the cavity control field enters as an effective standing-wave atom–cavity coupling parameter $\Omega_c = 2g\sqrt{n+1}$.

To examine the resulting PSHE displacement, we consider the transverse reflection of a probe field interacting with the cavity, which can induce a lateral shift in the reflected beam. The PSHE shift for a plane-wave probe component is evaluated using Eq. (15). In this configuration, the atomic ensemble—operating under an EIT scheme—is situated between two dielectric layers, and the probe beam impinges upon the structure at an angle θ_i relative to the surface normal, as illustrated in Fig. 1.

Figure 7 presents the influence of Doppler broadening on the PSHE for several intracavity configurations. Panels 7(a) and 7(b) show the transverse shift δ_p^+ in the absence of the microwave field ($\Omega_s = 0$) for cavity photon numbers $n = 0$ and $n = 10$, respectively. In both cases, the shift exhibits a distinct sign reversal at an incidence angle corresponding to the peak of the polarization contrast ratio $|R_s|/|R_p|$. Doppler broadening smooths the angular dependence and reduces the peak magnitude compared with the cold-atom scenario, although the key spin-dependent splitting remains clearly observable.

In Figs. 7(c) and 7(d), a weak microwave drive ($\Omega_s = 0.12\gamma$) is introduced. Under this condition, the magnitude of the PSHE shift is noticeably diminished and its variation with θ_i becomes more gradual. This occurs because the microwave-induced coherence alters the susceptibility of the Doppler-broadened medium, thereby weakening the effective anisotropy between the s- and p-polarized reflection channels that generates the spin–orbit interaction. Even so, the zero-crossing of δ_p^+ remains, indicating that Doppler effects modify but do not suppress the geometric origin of the PSHE.

A comparison of the four cases highlights several consistent trends. Increasing the photon number from $n = 0$ to $n = 10$ enhances the atom–cavity coupling and slightly increases the PSHE shift, despite the presence of Doppler broadening. Conversely, activating the microwave field generally reduces the displacement by diminishing the refractive index contrast required for strong spin-dependent beam steering. Overall, Fig. 7 demonstrates that although Doppler broadening smooths and weakens the PSHE response, the underlying angular dependence including the characteristic reversal linked to the ratio $|R_s|/|R_p|$ remains robust across all evaluated conditions.

Figure 8 depicts the density distribution of the PSHE transverse shift δ_p^+ as a function of the incident angle θ_i and the microwave field strength Ω_s. Panel 8(a) represents the case of zero intracavity photon number ($n = 0$), while panel 8(b) corresponds to a finite photon population ($n = 10$).

In Fig. 8(a), the behavior of PSHE is illustrated for the reference case of $n = 0$, corresponding to the vacuum-induced transparency under Doppler broadening. A sharp enhancement in the transverse shift is observed near $\theta_i \approx 39°$, where both positive and negative extrema are reached. The lateral displacement strongly depends on the microwave field Ω_s. For weak microwave fields, a slight increase in Ω_s enhances the PSHE within the transparency window. However, at higher values of Ω_s, the system transitions from a transparency regime to a gain-dominated regime, leading to a reduction in the magnitude of the PSHE. This indicates that spin-dependent shifts can be efficiently controlled using a weak microwave field.

Figure 8(b) shows the case of a higher intracavity photon number ($n = 10$) in the presence of Doppler broadening. Here, the maximum PSHE shift occurs at a slightly smaller incident angle, around $\theta_i \approx 35°$. For very small Ω_s, the transverse displacement is significantly enhanced due to the broadened zero absorption window associated with the increased photon number, reflecting the combined influence of microwave-induced coherence and cavity-assisted atom–photon interactions. As Ω_s increases further, the emergence of gain again suppresses the PSHE magnitude. Both positive and negative shifts are present, demonstrating that not only the magnitude but also the direction of the PSHE can be tuned via the microwave field and cavity parameters.

Overall, these results confirm that the PSHE can be effectively manipulated by adjusting the microwave Rabi frequency and the intracavity photon number, even in the presence of Doppler broadening. While Fig. 8(a) represents the baseline response without photon contribution, Fig. 8(b) highlights the robustness and tunability of the effect under modified conditions. In conjunction with Fig. 7, it is evident that the spin-dependent transverse shift is governed by both the incident angle and the applied microwave field, enabling precise control of vacuum-induced PSHE within a cavity-QED system.

6 Conclusions

In conclusion, the comprehensive analysis presented demonstrates that the PSHE in an atomic system can be robustly controlled via vacuum-induced transparency and spin-dependent light-matter interactions mediated by quantum vacuum fluctuations. The system exhibits a pronounced transparency window and steep dispersion near resonance, even in the absence of classical control photons, confirming the critical role of vacuum Rabi coupling. The angular dependence of Fresnel reflection coefficients reveals that maximal polarization anisotropy—and consequently enhanced spin-dependent beam shifts—occurs near the Brewster angle, establishing an optimal regime for strong spin–orbit interaction. Atomic number density significantly influences the PSHE behavior: high-density media amplify collective dipole–dipole interactions, resulting in sharp detuning-dependent variations and enhanced spin splitting, whereas dilute gases yield more stable, detuning-insensitive spin shifts governed primarily by interface geometry. Introducing a microwave coupling field modifies the transparency window by inducing gain, which can suppress the PSHE amplitude by reducing polarization-dependent reflectivity contrast. Furthermore, increasing the control field photon number broadens the transparency window and enhances the PSHE magnitude, though it reduces angular sensitivity due to gain-induced smoothing of optical anisotropy. Overall, these results elucidate the delicate interplay between quantum vacuum effects, atomic density, external coherent driving, and photon statistics in tailoring spin-dependent photonic phenomena, offering versatile avenues for tunable spin-optical devices and quantum information processing platforms.

Data availability Data that supports the finding will be available upon reasonable request to authors. The manuscript has associated data in a data repository.

References

1. S.E. Harris, Phys. Today **50**, 36 (1997)
2. M. Fleischhauer, A. Imamoglu, J.P. Marangos, Rev. Mod. Phys. **77**, 633 (2005). https://doi.org/10.1103/RevModPhys.77.633
3. H. Tanji-Suzuki, W. Chen, R. Landig, J. Simon, V. Vuletić, Science **333**, 1266 (2011)
4. J. Field, Phys. Rev. A **47**, 5064 (1993)

5. D. Schuster, A.A. Houck, J. Schreier, A. Wallraff, J. Gambetta, A. Blais, L. Frunzio, J. Majer, B. Johnson, M. Devoret et al., Nature **445**, 515 (2007)
6. G.S. Agarwal, J.Opt. Society America B **2**, 480 (1985)
7. R. Miller, T. Northup, K. Birnbaum, A. Boca, A. Boozer, H. Kimble, J. Phys. B: Atomic Molecular Opt. Phys. **38**, S551 (2005)
8. H. Toida, T. Nakajima, S. Komiyama, Phys. Rev. Lett. **110**, 066802 (2013)
9. Y.-J. Guo, W.-J. Nie, Chin. Phys. B **24**, 094205 (2015)
10. B. Hou, S. Wang, W. Yu, W. Sun, J. Phys. B: Atomic Molecular Opt. Phys. **39**, 2335 (2006)
11. H. Chen, X. Wang, I. Ahmed, X. Yao, Z. Wu, D. Zhu, Y. Zhang, Appl. Phys. B **120**, 765 (2015)
12. L.-G. Qin, Z.-Y. Wang, S.-C. Wu, S.-Q. Gong, H.-Y. Ma, J. Jing, Opt. Commun. **410**, 102 (2018)
13. J.-W. Fan, J. Xu, M.-T. Cheng, Y. Yang, Opt. Exp. **26**, 19498 (2018)
14. W.E. Lamb Jr., R.C. Retherford, Phys. Rev. **72**, 241 (1947)
15. J. Gea-Banacloche, M. Scully, M. Zubairy, Phys. Scr. **1988**, 81 (1988)
16. G. Nikoghosyan, M. Fleischhauer, Phys. Rev. Lett. **105**, 013601 (2010)
17. M. Onoda, S. Murakami, N. Nagaosa, Phys. Rev. Lett. **93**, 083901 (2004)
18. K.Y. Bliokh, Y.P. Bliokh, Phys. Rev. Lett. **96**, 073903 (2006)
19. J. Sinova, S.O. Valenzuela, J. Wunderlich, C. Back, T. Jungwirth, Rev. Mod. Phys. **87**, 1213 (2015)
20. S.O. Valenzuela, M. Tinkham, Nature **442**, 176 (2006)
21. F. Cardano, L. Marrucci, Nat. Photonics **9**, 776 (2015)
22. K.Y. Bliokh, F.J. Rodríguez-Fortuño, F. Nori, A.V. Zayats, Nat. Photonics **9**, 796 (2015)
23. M. Kim, Y. Yang, D. Lee, Y. Kim, H. Kim, J. Rho, Laser & Photonics Rev. **17**, 2200046 (2023)
24. L. Sheng, Y. Chen, S. Yuan, X. Liu, Z. Zhang, H. Jing, L.-M. Kuang, X. Zhou, Progress in Quantum Electronics , 100484 (2023)
25. S. Liu, S. Chen, S. Wen, H. Luo, Opto-Electron. Sci. **1**, 220007 (2022)
26. R.-G. Wan, M.S. Zubairy, Phys. Rev. A **101**, 033837 (2020)
27. J. Wu, J. Zhang, S. Zhu, G.S. Agarwal, Opt. Lett. **45**, 149 (2019)
28. M. Waseem, M. Shah, G. Xianlong, Phys. Rev. A **110**, 033104 (2024)
29. M. Abbas, Y. Wang, F. Wang, H.R. Hamedi, P. Zhang, Chaos. Solitons & Fractals **196**, 116292 (2025)
30. M. Abbas, P. Zhang, H.R. Hamedi, Phys. Rev. A **111**, 043708 (2025)
31. M. Abbas, W. Liu, P. Zhang, H.R. Hamedi, Annalen der Physik , e00194 (2025c)
32. M. Shuraim, M. Waseem, S. Qamar, M. Irfan, Phys. Rev. A **110**, 063717 (2024)
33. Z.A. Khan, A.A. Khan, Z. Ali, Rahmatullah, Ziauddin, S.-H. Dong, Physical Review A **112**, 013718 (2025)
34. M. Waseem, arXiv preprint arXiv:2512.14586 (2025)
35. L. Wu, H.S. Chu, W.S. Koh, E.P. Li, Opt. Exp. **18**, 14395 (2010). https://doi.org/10.1364/OE.18.014395
36. Y. Xiang, X. Jiang, Q. You, J. Guo, X. Dai, Photonics Res. **5**, 467 (2017)
37. M. Abbas, S.H. Asadpour, Ziauddin, P. Zhang, J. Ruseckas, H.R. Hamedi, Physical Review A **110**, 023730 (2024)
38. L. Zhang, F. Zhou, Y. Niu, J. Zhang, S. Gong, Opt. Commun. **284**, 5697 (2011)
39. E. Fermi, Rev. Mod. Phys. **4**, 87 (1932)
40. G. Agarwal, T.N. Dey, Phys. Rev. A **68**, 063816 (2003)